# Design and Analysis of an Event Camera Payload for Space-Based Object Detection on the EventSat 6U CubeSat Mission

**Sydney Dolan[1*], Lara Schuberth[1], Rugved Arge[1], Ramón María García Alarcia[1], Vincenzo Messina[1], Clemente J. Juan Oliver[1], Francesco Salmaso[1], Jaspar Sindermann[1], Federico Sofio Avogadro[1], Alessandro Golkar[1]**

[1]Technische Universität München
Caroline-Herschel-Str. 100, 85521 Ottobrunn, Germany
Phone: +49 89 289 55752, Mail: sydney.dolan@tum.de

**Key words**: technology demonstration, event cameras, baffle

## ABSTRACT

The EventSat mission is a technology demonstration mission of a 6U CubeSat by Technical University of Munich to apply event cameras for resident space object detection. Event cameras are asynchronous sensors that detect changes in pixel brightness, providing data updates at a microsecond temporal resolution with low power consumption. We perform an initial analysis of the limiting apparent visual magnitude for the Prophesee EVK4, accounting for parameters like dark current, quantum efficiency, and optic aperture diameter. Initial simulations estimate that the sensor will be able to detect visual magnitudes up to 7.7. Then, we perform a parametric analysis relating the qualities of different resident space objects like their speed, brightness, and size; and the optic qualities of the sensor like its f-number and contrast threshold. This analysis constraints the types of detectable space objects for the planned mission. Finally, we discuss the development of a single-stage baffle for our event camera. Baffles reduce stray light from nearby bodies, which is important for our mission to detect dim objects within its limiting magnitude. We estimate initial baffle sizing, and conduct trade-off studies on vane dimension, placings, and exclusions angles. These results help define the mission's pointing and operational requirements.

## 1. INTRODUCTION

Ground-observations of space objects are limited by atmospheric interference, weather conditions, and line-of-sight constraints, reducing their effectiveness for comprehensive space situational awareness. Space-based observers have the potential to resolve some of these limitations, but additional research is required to develop efficient detection capabilities.

One promising method for space-based observation involves the use of event cameras. Event cameras are a specialized type of camera that use a sensor that can capture very fast motions through asynchronous, microsecond, updates. Event cameras track these fast motions by monitoring the variations in light intensity within a scene. Unlike traditional frame-based cameras, event cameras update pixels asynchronously, with each pixel independently detecting changes in brightness. When the change in intensity at a pixel exceeds a predefined threshold, an event is generated, capturing the pixel's location, timestamp, and polarity of the change [1]. Because events are triggered only by changes in brightness in a scene, most pixels remain inactive when imaging the night sky; suggesting event-based systems for space applications will have lower power consumption and data throughput than traditional cameras. To formalize these potential benefits, there is a need to develop additional algorithmic and processing architectures compatible with event-based sensing.

This work aims to analyze the constraints and operational context of event-based sensing for CubeSat platforms. In this paper, we use EventSat as a representative mission for

* Corresponding Author

analysis. EventSat is a 6U CubeSat by the Technical University of Munich designed to demonstrate the effectiveness of event cameras for space-based observation of stars, satellites, and other space objects [2]. Using a 4th generation commercial off-the-shelf event camera, the CubeSat will collect space-based observations of the night sky and demonstrate artificial intelligence algorithms for space object detection.

In this work, we present the design and development process of the EventSat payload. In Section 2, we provide an overview of the overall spacecraft design, mission concept of operations, and mass and power budgets. In Section 3, we delve deeper into the payload design and present the initial study evaluating the theoretical detection capabilities. Then, in Section 4, we present our parametric analysis comparing resident space object characteristics and the optics characteristics of our payload. Using the sizing constraints derived by our parametric study, we present the optic and baffle design in Section 5. Finally, Section 6, contains a summary of the work completed thus far and a discussion of the remaining work needed to bring the project to completion. In this paper, we show maturation of the EventSat payload design, and significant progress towards integration and testing of the flight payload.

## 2. CUBESAT OVERVIEW

EventSat relies on two 3U Solar panels, and two 6U solar panels on the exterior of the spacecraft for power generation. Additionally, the planned electrical power system (EPS) design features two Lithium-Ion batteries for energy storage. For communications (TT&C), the satellite uses UHF and S-band transceivers and antennas to communicate with ground. An onboard computer (OBC) will control all transitions between different operational modes of the spacecraft. The attitude determination and control system (ADCS) is composed of 4 reaction wheels, a three-axis magnetorquer, a star sensor, two sun sensors and a three-axis magnetometer. The payload design relies on a Nvidia Jetson Orin Nano for computing and observation data storage. Additional details about the payload specifications can be found in Section 6. A heat sink and mount attached to the Nvidia Jetson Orin Nano is used for thermal control.

### *Concept of Operations*

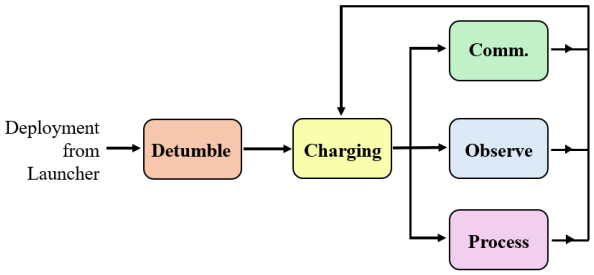


*Figure 1: Interaction Between Different Concept of Operations Modes*

After successful deployment from the CubeSat deployer into a Sun Synchronous Orbit, EventSat will enter a detumbling mode where the spacecraft dumps excess angular momentum and stabilizes the orientation of the spacecraft. Following detumbling mode EventSat enters Charging. From there EventSat can enter three further modes: (1) observe mode, (2) process mode and (3) communication mode. If there is a fault in any of these modes, EventSat will enter a safe mode for troubleshooting.

Charging mode serves to replenish the batteries and restore the spacecraft to power and thermal equilibrium. This mode orients EventSat so that the solar panels are faced towards the sun to maximize power generation across multiple faces. In observe mode, the event camera is turned on and records event data. Observe mode orients EventSat such that the event camera points radial, so that the payload can fulfill the imaging mission requirements. Process mode serves to post-process the event data and integrate it with other spacecraft information for downlink. Process mode puts EventSat in the same orientation as charging mode. Communication mode is used for EventSat to downlink telemetry and observation taken from the event camera to the ground station, and to receive telecommands sent from the ground. This mode orients EventSat such that the UHF and S-band antennas point nadir.

*Table 2: EventSat Power Consumption*

| ConOps Mode | Case | OBC (W) | TT&C (W) | ADCS (W) | Payload (W) | EPS (W) | Total (W) |
|---|---|---|---|---|---|---|---|
| Observe | Sun | 0.40 | 0 | 2.86 | 11.5 | 3.18 | 17.94 |
| | Eclipse | 0.40 | 0 | 2.52 | 11.5 | 3.13 | 17.55 |
| Communica-tion | Sun | 0.40 | 15.7 | 12.32 | 0 | 5.23 | 33.65 |
| | Eclipse | 0.40 | 15.7 | 11.97 | 0 | 5.17 | 33.24 |
| Processing | Sun | 0.40 | 0 | 2.86 | 7 | 2.51 | 12.77 |
| | Eclipse | 0.40 | 0 | 2.52 | 7 | 2.45 | 12.37 |
| Charging | Sun | 0.40 | 0 | 2.86 | 0 | 1.46 | 4.72 |
| | Eclipse | 0.40 | 0 | 2.52 | 0 | 1.40 | 4.32 |
| Safe | Sun | 0.40 | 4.5 | 2.59 | 0 | 2.09 | 9.58 |
| | Eclipse | 0.40 | 4.5 | 2.59 | 0 | 2.09 | 9.58 |
| Detumbling | Sun | 0.29 | 0 | 1.25 | 0 | 1.12 | 2.66 |
| | Eclipse | 0.29 | 0 | 0.90 | 0 | 1.14 | 2.33 |

### *Mass and Power Budget*

Full details of the subsystem masses and contingencies are included in Table 1. Contingencies were added to account for additional interfaces (e.g. wiring, connecting supports) that have not yet been modelled at this stage of design. Even with these additional mass contingencies, the total projected mass of the satellite is still less than the mass requirement of 7980 grams [3]. The TT&C, EPS, and OBC subsystems were allocated small contingencies due to their interfaces being at a more advanced stage in design than other subsystems.

*Table 1: EventSat Mass Budget*

| System | Mass Fraction (%) | Mass (g) | Contingency (%) | Mass + Contingency (g) |
|---|---|---|---|---|
| ADCS | 9.1 | 615 | 20% | 738 |
| Payload | 22.6 | 1537.1 | 20% | 1844.5 |
| OBC | 1.9 | 130 | 10% | 143 |
| EPS | 42.1 | 2855.3 | 5% | 2998.1 |
| TT&C | 8.9 | 603.9 | 10% | 664.3 |
| Thermal | 0.7 | 48 | 20% | 57.6 |
| Structure | 14.7 | 1000 | 20% | 1200 |
| Total | 100 | 6789.3 | -- | 7645.5 |

Table 2 contains the preliminary power consumption estimations for the power budget for EventSat. Communication mode results in the highest power consumption for the mission, followed by observation mode. Although both modes consume significant power, they are designed to occur for only brief periods each day. As a result, we estimate the EPS subsystem will be able to effectively compensate via charging mode and ensure that all subsystems remain powered and planned mission operations can continue without interruption.

## 3. PAYLOAD DETECTABILITY STUDY

To determine the camera's ability to detect objects of varying brightness, we calculated the limiting magnitude threshold for several proposed lens apertures. The limiting magnitude threshold defines the faintest apparent visual magnitude detectable by the event camera payload. Objects dimmer than the limiting apparent visual magnitude will not be seen by the event camera. Apparent visual magnitude is dependent on the observed flux of an object, $\Phi$, relative to the flux of some reference star of known magnitude, $\Phi_0$. Using the A0 Vega star as a reference, with magnitude $m_0$ [4], and a range of target visual magnitudes, $m$, we calculated the corresponding flux incident on the sensor.

$$\Phi = \Phi_0 10^{-\frac{m-m_0}{2.5}} \qquad (1)$$

Then, we use convert the flux, $\Phi$ and measured in $Wm^{-2}nm^{-1}$, into the number of detected photons per second $N$ using Planck's relation ($E = hc/\lambda$) and Equation 2. The total number of photons, $N$, is determined

based on the event camera's collecting area, the filter bandpass, $w$, the aperture area, A, and the quantum efficiency of the camera, $QE$.

$$N = (\Phi/\mathrm{E}) \cdot A \cdot \mathrm{QE} \cdot w \quad (2)$$

To estimate the signal received by the camera, we determine how many photons fall on each pixel by distributing the total photon count over the expected pixel footprint of an A0 star, $\beta$. This per-pixel photon count is called by the integration time, to obtain the signal, as shown in Equation 3.

$$S = (N/\beta) * t \quad (3)$$

The total noise in the event camera is calculated via Equation 4.

$$\nu = \sqrt{\nu_{DN}^2 + \nu_{RN}^2 + \nu_{SN}^2} \quad (4)$$

The square root of the signal, $S$, gives the shot noise, $\nu_{SN}$. The readout noise, $\nu_{RN}$, is dependent on the charge conversion efficiency, CCE, and the standard deviation of the pixel signal, $\sigma$.

$$\nu_{RN} = \frac{CCE\ \sigma}{\sqrt{2}} \quad (5)$$

The dark noise, $\nu_{DN}$, is derived from the dark current, which is measured by taking dark frames with a thermal control system. Based on performance data from comparable imaging systems [5], the dark current, $i_{DN}$, has been approximated as 1.095 $e^-/s$ .

$$\nu_{DN} = \sqrt{i_{DN} t} \quad (6)$$

Using these noise estimates, we can calculate the signal-to-noise ratio, SNR, of the event camera, as shown in Figure 2.

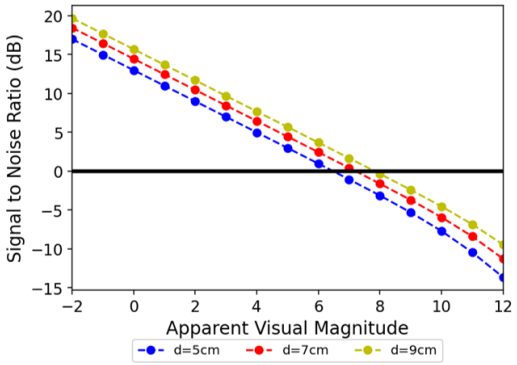


*Figure 2: Limiting Visual Magnitude*

A positive SNR value can be considered a general indication of increased likelihood of star detection; however, the actual detection probability depends on factors such as false alarm rates, and signal processing algorithms, which are beyond the scope of this paper. Thus, Figure 2 should be considered in this context. We evaluate three possible aperture diameters, $d$, of 5,7, and 9 centimeters. As suggested by Eq. 2, the larger the aperture, the more photons that can arrive to the image sensor, thereby improving detectability. However, due to the constraints of the CubeSat form factor, we are limited to a maximum aperture diameter of 9 cm. This is an upper bound that represents the best-case scenario. While a larger aperture would be ideal for improved sensitivity, practical considerations such as available space and other components inside the CubeSat impose strict physical limitations.

The intersection of the SNR slope curve with the 0 value indicates the limiting magnitude for different aperture values. This corresponds to magnitudes of 6.27, 7.07 and 7.68 for the apertures considered. As a benchmark, commercial star trackers typically have limiting magnitude thresholds around 6, which enables them to detect sufficient stars in their field of view for reliable attitude determination [6]. These initial limiting magnitude threshold calculations serve to validate the theoretical feasibility of event camera space object detection. We used rough approximations for dark current, charge collection efficiency, which may introduce some uncertainty into the results. Additionally, true flux calibration spans multiple spectral bands; thus actual event camera performance could be underestimated as contributions from wavelengths outside of the visible range are not accounted for. Future iterations of this analysis will develop more realistic noise modeling and evaluate the impact of these additional wavelength bands. It is important to note that the event camera exhibits peak quantum efficiency within the visible spectrum, and as such, this analysis captures the dominant spectral contribution to the signal.

## 4. PIXEL RESPONSE PARAMETRIC ANALYSIS

Accurate predictions of the event cameras sensitivity require a more detailed analysis that accounts for the pixel architecture. A pixel within an event camera has three stages: a logarithmic photoreceptor, a change amplifier, and a comparator stage

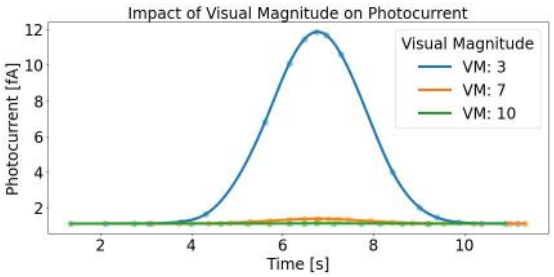


*Figure 4: Visual Magnitude Impact on Photocurrent*

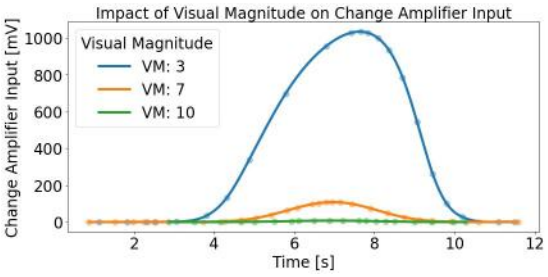


*Figure 5: Visual Magnitude Impact on Change Amplifier*

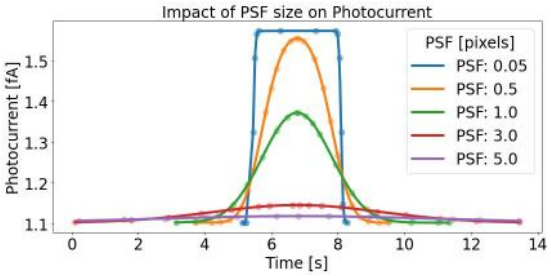


*Figure 6: PSF Impact on Photocurrent*

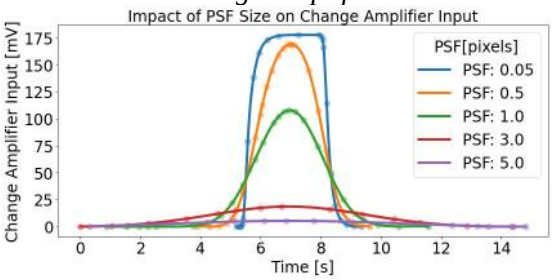


*Figure 7: PSF Impact on Change Amplifier*

[7]. A simplified version of this circuit design is shown in Figure 3.

First, the photoreceptor converts incoming light or photons into an electrical signal. As light strikes the photoreceptor, it excites electrons, creating charge carriers that produce a photocurrent. The magnitude of the photocurrent is directly related to the intensity of the incoming light, making it an effective metric to evaluate the dynamic range of the proposed event camera and optics system.

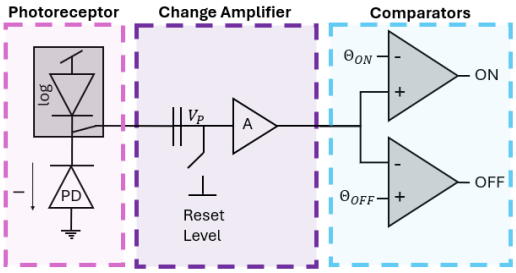


*Figure 3: Pixel Circuit Design*

After the photoreceptor, a change amplifier converts the generated photocurrent into an output voltage ($V_p$). This voltage is useful for understanding the amplitude of the accumulated signal, to determine the detection thresholds possible with the camera.

In the comparator stage, the voltage signal is continuously monitored and compared to a reference level stored in analog memory, corresponding to the signal level of the last reported event [7]. An event is generated when the log intensity increases or decreases by a tunable global threshold value. This event is recorded and read off the chip by the peripheral circuits [7]. Following the event reporting, the pixel enters a refractory period, during which it ignores further signal changes until its reference level is reset; after this reset, the pixel resumes monitoring and reports subsequent changes relative to the updated reference.

Using the theoretical event pixel model developed by [7], we performed a parametric study to evaluate the performance limits of our proposed event camera and optics system. Table 3 contains the key assumptions of our model. The parametric study considers that the point spread function (PSF) passes through the center of the single pixel.

*Table 3: Key Assumptions*

| | |
|---|---|
| Background | 20 m/arcsec$^2$ |
| ON threshold | 0.2 |
| OFF Threshold | 0.8 |
| Bandwidth | 1K |
| Refraction period | 5ms |
| Array Size | 5 |
| Focal length | 35 mm |
| F-number | 1.8 |

First, we delved deeper into the pixel's sensitivity to objects of different magnitudes.

Figures 4 and 5 demonstrate the results for a resident space object (RSO) with a point spread function of 1, and a speed of 15 arcsec/s. Lower visual magnitudes correspond to brighter objects, and subsequently larger peak photocurrents and change amplifier magnitudes. When looking beyond the comparator stage and towards actual generated events, the event camera optics generates events for visual magnitudes 3 and 7, but not for 10.

This means that an object with a visual magnitude of 10 is not visible for the sensor. Applications for space situational awareness deal in particular with scenarios involving dim lighting conditions and low contrast. One possible approach to detecting objects with higher visual magnitudes is to further reduce the threshold settings for event generation. For the presented case - even at the lowest possible bias setting of the tool, no events are generated. Another way of increasing the photocurrent is by decreasing the PSF, which will be described next. This would fundamentally alter the object's properties, meaning it could no longer be considered the same object.

Next, we evaluate the impact of point spread function size on the pixel response. The point spread function, describes how a point source of light, like a star, is spatially distributed on the image sensor due to diffraction and optical aberrations. Figures 6 and 7 show the impact of PSF size on the photocurrent generation and change amplifier response for a RSO with visual magnitude 7, and speed of 15 arcsec/s. For smaller PSF parameters, there is more photocurrent generated. However, the generation interval itself is smaller, indicating a smaller period where the PSF is registered by the sensor. A similar trend occurs with the PSF and the change amplifier input; the smaller the PSF value, the more concentrated the change amplifier input. Unlike the photocurrent, the change amplifier curves exhibit a noticeable asymmetry at smaller PSF values. This asymmetry can be attributed to increased sensitivity to noise and potential non-linearities in the amplifier response.

Finally, we evaluated the impact of speed on the pixel response. We evaluated the impact of speed on a bright object of visual magnitude 3 and PSF of 1. Table 4 shows the comparison of different speeds on resultant photocurrent.

*Table 4: Impact of Object Speed on Resident Space Object Detection*

| **Speed (arcsec /sec)** | **Peak Photocurrent (fA)** | **Peak Time (s)** | **Photocurrent Standard Deviation** |
|---|---|---|---|
| 1.8 | 11.83 | 56.26 | 4.07 |
| 15.0 | 11.83 | 6.75 | 4.58 |
| 100.0 | 11.83 | 1.01 | 4.31 |
| 200.0 | 11.83 | 0.51 | 4.35 |

An object of visual magnitude 3 will generate the same peak photocurrent, regardless of speed. However, the duration of the signal varies significantly, as shown by the relative peak positions. These results are intuitive, as slower objects will remain in the camera's field of view for a longer duration, causing their signal to build up more gradually and take more time to reach its peak.

## 5. PAYLOAD MECHANICAL DESIGN

To block stray light from entering the camera, we have also designed a baffle to enhance image contrast and signal fidelity. Baffles are mounted around the lens and camera assembly, extending outward to preserve the field of view. Key design parameters are listed in Table 5.

*Table 5: Baffle Design Constraints*

| | |
|---|---|
| Sun Exclusion Angle | 34° |
| Internal Pupil Diameter | 15 mm |
| Camera Effective FOV | 28.1° |
| Tuna Can Inner diameter | 93 mm |
| Tuna Can Depth | 78 mm |

The tuna can refers to the maximum cross-sectional size available for payload components, typically reserved for deployable external facing hardware. By using this available space for the baffle, we can increase the available space for the optics, thereby improving the camera sensitivity. To determine

*Table 6: Summary of Baffle Design Iterations*

| Parameter | Iteration 1 | Iteration 2 (Selected) | Iteration 3 |
|---|---|---|---|
| **Annular Depths** ($J_b$/ $J_t$) | 13 mm / 10 mm | 12 mm / 6 mm | 8 mm / 4 mm |
| **Outer Radius** | 44.685 mm | 44.6965 mm | 42.409 mm |
| **Exclusion Angle** | 35° | 34° | 32.5° |
| **Baffle Length** | 66.67 mm | 70.71246 mm | 77.56 mm |
| **Number of Vanes** | 4 | 6 | 9 |
| **Outcome** | Fewer components and a shorter design, but inadequate stray light suppression. | Achieves a strong balance between effective stray light control and adherence to geometric constraints. | Offers enhanced stray light rejection but adds complexity and tight tolerances for assembly. |

the baffle specifications, we applied the geometric modeling techniques outlined in Rohrbach's analytical framework for baffle design [8].

To identify an optimal baffle configuration, three design iterations were carried out—each varying in sun exclusion angle, vane count, annular depth, and overall dimensions. The goal was to maximize stray light rejection while staying within the mechanical constraints of the tuna-can volume and avoiding excessive design complexity.

Table 6 summarizes the evaluated parameters and outcomes for each configuration. Ultimately, Iteration 2 was chosen as the final design. We aimed to maximize the sun exclusion angle when possible, as the sun exclusion angle is the minimum angular distance between the optic line of sight and the sun. Iteration 2 also fit within the available tuna-can depth available for the baffle, and did not introduce additional unnecessary complexity. By accommodating six vanes and a baffle length of 70.71 mm, this configuration provided robust stray light attenuation while still allowing for safe manufacturing tolerances and mechanical integration. It also leveraged the maximum usable outer radius within the tuna-can, further enhancing its effectiveness against off-axis light intrusion.

The relatively large sun exclusion angle of the baffle introduces operational imitations. Specifically, it defines a conical region around the optical axis into which the Sun must not enter in observation periods. This constrains the satellite's permissible pointing directions and may limit imaging opportunities when targets lie close to the Sun's apparent position. In this way, the exclusion angle is not only a geometric outcome but also a strategic design parameter that ties together optical, mechanical, and operational considerations.

Figure 8 shows the final selected baffle design, emphasizing the slenderness of the vanes, a direct consequence of employing Rohrbach's adjusted recursive equations for stray light mitigation [8]. From a theoretical perspective the thin vane structure minimizes stray light, but the practical implementation introduces considerable manufacturing challenges. The expected fabrication tolerances of ±0.25 mm require careful machining. Furthermore, precise vane height is crucial as variations from intended dimensions carry significant risks. If the vanes are too tall, they might intrude into the optical path, leading to unwanted vignetting and data loss. Conversely, shorter vanes compromise the baffle's effectiveness in blocking

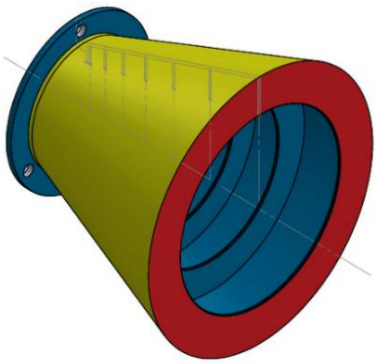

*Figure 8: Baffle Design*

stray light and reducing internal reflections. The baffle is fixed to the lens via a C-mount. Future iterations of the payload design will develop interfaces to fix the baffle/lens system onto the CubeSat rods.

## 6. CONCLUSION

This paper has provided an update on the development of the EventSat mission. We have provided mass and power budgets for the current design phase. Through detailed analyses, including a limiting magnitude estimation and parametric studies of both object and sensor characteristics, this paper has defined the operational boundaries for object detectability. The parameter study revealed that objects with visual magnitudes of 3 and 7 generate events, while objects with a visual magnitude of 10 do not produce any events and are therefore not detectable by the camera.

Additional work is required to validate the baffle's performance for integration into a CubeSat platform. Future work will focus on structural and environmental testing to ensure mechanical integrity under launch and orbital conditions. To quantify the baffle's effectiveness against scattering and internal reflections stray light analysis will be performed. A support frame must be designed to mechanically interface the baffle and lens assembly with the CubeSat's structural rods. The combined baffle-support system will undergo structural, vibrational, and thermal analyses. These efforts are critical to advancing the current design from a theoretical model to a fully flight-qualified subsystem capable of supporting high-fidelity imaging in space.

## ACKNOWLEDGEMENTS

Sydney Dolan and Lara Schuberth are funded by the Federal Ministry for Economic Affairs and Climate Action (BMWK) through the German Aerospace Center (DLR) (Grant No. 50LZ2402). We would like to thank Scott Rohrbach for discussion and feedback on our baffle design. Additionally, the team of students that have supported EventSat is larger than the number of authors listed in this paper, we sincerely thank all students involved for their efforts in the overall development.

Gefördert durch:

aufgrund eines Beschlusses
des Deutschen Bundestages

## REFERENCES

1. Gallego, G., Delbrück, T., Orchard, G., Bartolozzi, C., Taba, B., Censi, A., ... & Scaramuzza, D. (2020). Event-based vision: A survey. *IEEE transactions on pattern analysis and machine intelligence*, *44*(1), 154-180.
2. Schuberth, L., Messina, V., Alarcia, R. M. G., Sindermann, J., Nezhad, K. B., Velayos, R. A., ... & Golkar, A. (2024). Leveraging event-based cameras for enhanced space situational awareness: A nanosatellite mission architecture study. In *75th International Astronautical Congress (IAC)*.
3. Johnstone, A. (2020). CubeSat Design Specification,. In California Polytechnic, San Luis Obispo
4. Colina, L., Bohlin, R., & Castelli, F. (1996). Absolute flux calibrated spectrum of Vega. *Instrument Science Report CAL/SCS-008, Space Telescope Science Institute*.
5. Miguel, N. V. M. P., Gordo, P., & Gafeira, R. J. M. (2021). *Feasibility study of using a satellite Startracker for space debris detection on LEO orbits* (Master's thesis).
6. Aaron J. Swank. (2022). SWIR Star Tracking. *NASA Technical Report, NASA Glenn Research Center*.
7. McReynolds, B., Graca, R., Oliver, R., Nishiguchi, M., & Delbruck, T. (2023, September). Demystifying event-based sensor biasing to optimize signal to noise for space domain awareness. In *Advanced Maui Optical and Space Surveillance Technologies Conference (AMOS)*. University of Zurich.
8. Rohrbach, S. O. (2023, October). Corrected recursive equations for vane aperture sizes and locations in one-and two-stage stray light baffle systems. In *Earth Observing Systems XXVIII* (Vol. 12685, pp. 24-36). SPIE.